Nano Research

Open Access

Research Article

A sensing-storage monolithically integrated system based on P3HT OTFT for wearable physiological sensing

Yuwen Li[1,§], Qiang Li[1,§]✉, Lifeng Ding[2], Yuanzheng Cao[1], Hui Gao[1], Jianan Ma[1], Tsuyoshi Minami[3]✉, and Shengbo Sang[1]✉

[1] *Shanxi Key Laboratory of Artificial Intelligence & Micro Nano Sensors, College of Integrated Circuits, Taiyuan University of Technology, Taiyuan 030024, China*
[2] *Department of Chemistry and Chemical Engineering, Taiyuan Institute of Technology, Taiyuan 030008, China*
[3] *Institute of Industrial Science, The University of Tokyo, 4-6-1 Komaba, Meguro-ku, Tokyo 153-8505, Japan*
§ *Yuwen Li and Qiang Li contributed equally to this work.*

Cite this article: *Nano Research*, **2026**, *19*, 94908532. https://doi.org/10.26599/NR.2026.94908532

ABSTRACT: Wearable health monitoring systems require seamless integration of sensing and memory functionalities for real-time physiological signal acquisition and processing. However, conventional approaches relying on hybrid integration of rigid silicon-based memory with flexible sensors suffer from mechanical mismatch and complex interfacing, limiting their practicality in continuous physiological monitoring. Here, we present a sensing-storage monolithically integrated system fabricated through low-cost solution spin-coating, which combines a flexible floating-gate organic thin-film transistor (FG-OTFT) memory with an OTFT pressure sensor. The pressure sensor exhibits a wide operating range of 0–40 kPa, a fast response time of 34 ms, and stable performance after 5000 bending cycles and over temperatures from −20 to 60 °C. When conformally attached to the finger joint, wrist, and human throat, the device delivers distinct current variations that faithfully track joint bending angles and intermittent coughing. The integrated floating-gate memory exhibits a large memory window of 18 V under ±80 V program/erase biases, a retention time exceeding 10^5 s, and robust operation after 3000 bending cycles. A 1 × 9 memory array is used to store 7-bit ASCII-encoded characters with two additional check bits, and the stored information is wirelessly transmitted via Bluetooth low energy to a mobile application. Comparative analysis shows that the integrated system offers a shorter response time and longer data retention than previously reported OTFT-based pressure sensors and organic memories used for physiological monitoring. These results highlight a low-cost, fully flexible, and application-oriented platform for wearable electronic skins capable of simultaneous physiological sensing, data storage, and intuitive visual readout.

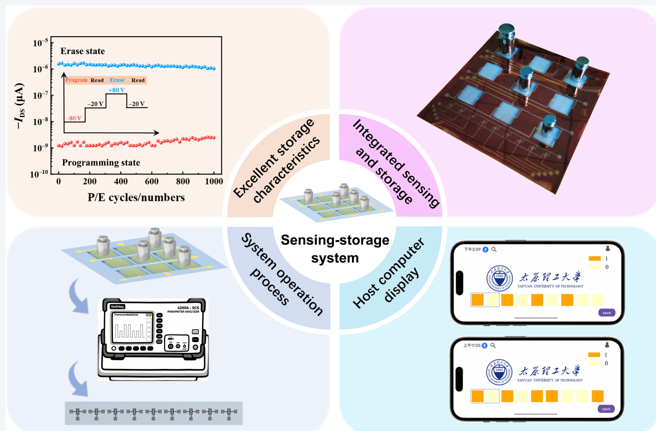

KEYWORDS: poly(3-hexylthiophene) (P3HT), floating-gate transistor memory, organic thin-film transistor pressure sensor, wearable physiological monitoring

1 Introduction

Flexible electronic skin [1–9], as a key component of next-generation wearable devices and bio-inspired robots, must satisfy stringent requirements for high-speed sensing [10–16] and real-time storage [17, 18] of dynamic signals. Such biomimetic systems are expected to capture multimodal physical signals including pressure [19–22], temperature [23], and strain [24] in real time, while millisecond-level data buffering and processing are performed by embedded memory units. Among these modalities, pressure sensing [25–28] plays an indispensable role in perceiving physical interactions and environmental contact, with critical applications in pulse monitoring, tactile feedback, and human-machine interfaces.

Received: December 24, 2025; **Revised:** February 1, 2026
Accepted: February 3, 2026

✉Address correspondence to Qiang Li, liqiang02@tyut.edu.cn; Tsuyoshi Minami, tminami@g.ecc.u-tokyo.ac.jp; Shengbo Sang, sunboa-sang@tyut.edu.cn

High-performance flexible pressure sensors are required to exhibit high sensitivity, a broad detection range, and excellent cycling stability. Organic thin-film transistor-based pressure sensors [29–31] have emerged as an ideal choice due to their intrinsic signal amplification capability, low power consumption, and excellent mechanical flexibility. This capability provides essential technical support for high-fidelity real-time monitoring [32–34] and accurate perception [35] of physiological signals such as blood pressure, respiratory rate, and muscle activity. However, current integration strategies which typically rely on rigid silicon-based memory combined with flexible sensors are hindered by several major drawbacks. First, significant mismatch in Young's modulus between rigid memory chips and flexible substrates leads to stress concentration under bending, resulting in fracture of metallic interconnects or interfacial delamination. Second, heterogeneous integration requires complex interposers and packaging techniques, which not only increase system thickness but also introduce additional contact resistance and signal latency. Furthermore, the inclusion of rigid components markedly reduces the overall flexibility of the system, severely compromising conformability and comfort when applied to curved surfaces such as human joints. These limitations render existing designs unsuitable for applications demanding long-term stability, such as medical monitoring [36–38], highlighting the urgent need for novel fully flexible integrated [39, 40] solutions.

To achieve high-performance monolithic perception-storage integrated systems, the design of memory devices [41–43] is crucial. The floating-gate organic thin-film transistor [44–49] memory [50–53] has emerged as an ideal candidate due to its distinctive advantages: Firstly, its solution-processed multilayer organic structure (tunneling layer/floating gate/blocking layer) [52] exhibits excellent mechanical flexibility, maintaining stable performance even after repeated bending cycles. Its Young's modulus compatibility with flexible sensor materials effectively mitigates interfacial stress issues inherent in heterogeneous integration. Secondly, this integrated architecture significantly shortens signal transmission paths, markedly enhancing system response speed. Most importantly, this intrinsically compatible design ensures interfacial stability under bending strain, fundamentally avoiding delamination and complex interconnections caused by mechanical mismatch in conventional hybrid integrated systems. These characteristics enable floating-gate organic thin-film transistor (FG-OTFT) memory to effectively overcome the mechanical mismatch between conventional rigid memory and flexible sensors, providing a critical device-level foundation for highly reliable flexible electronic skin. Currently, research on flexible floating-gate transistor memory has attracted broad attention. For instance, Nam et al. successfully developed an intrinsically stretchable polymer memory transistor with outstanding mechanical properties. Their work innovatively employed a silver nanoparticle/elastomer composite as the floating gate layer, enabling the device to simultaneously achieve high flexibility and stretchability [52].

Although flexible FG-OTFT memories possess intrinsic flexibility, their fabrication has traditionally relied on high-cost vacuum deposition or photolithography techniques, which limits their scalability and adaptability for large-area electronic skin applications. Therefore, developing low-cost, scalable fabrication technologies has become a critical challenge for advancing the practical implementation of flexible memory devices. To address this, Chen et al. developed a flexible floating-gate organic field-effect transistor memory using a one-step blade-coating strategy. This device demonstrated reliable charge storage characteristics after repeated programming and erasing operations, along with excellent data retention capability [54]. Similarly, Kim et al. proposed a fully solution-processed, low-cost approach for fabricating high-performance n-channel organic transistor memory devices based on organic materials and direct printing techniques [55]. Concurrently, significant progress has been made in flexible OTFT-based pressure sensors [56, 57]. These sensors, leveraging their inherent advantages of flexibility, lightweight nature, and large-area manufacturability, demonstrate significant application potential in fields such as electronic skin, health monitoring, and human-computer interaction. Sun et al. successfully fabricated an extended-gate OTFT pressure sensor using a simple printing method [58], while Cheng et al. developed a carbon nanotube polyethylene terephthalate (CNTs-FET) pressure sensor featuring a micro-structured pyramidal top-gate electrode [59]. Nevertheless, no prior study has reported the successful integration of FG-OTFT memory with sensing modules to achieve a complete signal perception–storage process. To bridge this gap, this study proposes a sensing-storage monolithically integrated system fabricated entirely through low-cost solution spin-coating. The system combines a floating-gate organic thin-film transistor memory with a flexible pressure sensor. Considering both process compatibility and integration requirements, an OTFT-based flexible pressure sensor was selected as the sensing unit. The poly(3-hexylthiophene) (P3HT)-based OTFT pressure sensor used in this work was fabricated based on an established and well-optimized process from our research group. It exhibits high sensitivity and fast response characteristics, with its detailed structural design and performance characterization reported in Ref. [60]. This approach ensures the reliability of the sensing unit and allows this study to focus on the innovative integration of perception and memory within a single system.

This study presents a low-cost solution spin-coating approach for fabricating flexible floating-gate organic thin-film transistor memories for data storage in electronic skin devices. These memories were monolithically integrated with flexible OTFT pressure sensors to construct a unified perception–storage system. The fabricated memory devices exhibited a large memory window of 18 V under ±80 V programming/erasing voltages, along with a long charge retention time exceeding 10^5 s at a readout condition of $V_G = V_{DS} = -20$ V. Moreover, the memory transistors demonstrated excellent mechanical durability, maintaining stable performance after 3000 bending cycles, as well as remarkable environmental stability across varying temperatures and high device-to-device uniformity. Based on this process, a 1 × 9 memory array was further fabricated and integrated with a flexible OTFT pressure sensor array to form a monolithic perception–storage system. This system successfully achieved the storage of 7-bit binary-encoded data based on the ASCII standard, including upper- and lower-case letters, digits 0–9, and common punctuation marks, with the first two bits reserved as check bits. To validate its practical applicability, a customized data acquisition circuit was developed. This circuit captures current signals corresponding to different pressure levels through the OTFT pressure sensor, controls the programming/erasing operations of the memory array, and enables wireless data transmission via a Bluetooth module. Test results confirmed the reliable signal transmission performance of the integrated system. This work not only provides a feasible technical pathway for the design of perception–storage integrated systems, but also offers valuable insights for the development of future flexible electronic devices.

2 Experimental

2.1 Materials

All materials used in the experiment were commercially procured: Semiconductor material P3HT (molecular weight: 50 kDa, PDI = 1.2) and gold nanoparticle solution were purchased from Sigma-Aldrich; polymer materials including polyvinyl alcohol (PVA) (molecular weight: 130 kDa, PDI = 2.2) and 1,2-dichlorobenzene (AR, 99%) were sourced from Shanghai McLean Biochemical Technology Co., Ltd.; poly(p-xylene) (Parylene) (molecular weight: 208.30) was provided by Shanxi Demao Hongke Trading Co., Ltd.; flexible substrate material PET film (thickness 0.125 mm) was procured from Shenzhen Ruige Ruis Technology Co., Ltd. All chemical reagents and materials were used directly without further purification.

2.2 Device fabrication

In this study, a bottom-gate top-contact floating-gate organic thin-film transistor memory was fabricated on a flexible PET substrate. The detailed fabrication process was described as follows: A 3 cm × 3 cm PET substrate was first coated with a 30 nm-thick gold film via magnetron sputtering (VTC-600-2HD, Shenyang Kejing Automation Equipment Co., Ltd.) to serve as the gate electrode. The substrate was then ultrasonically cleaned (LE204E, Mettler Toledo Instrument Co., Ltd.) sequentially in ethanol and acetone, rinsed thoroughly with deionized water, and dried under a nitrogen stream. To enhance the hydrophilicity of the substrate, it was treated with oxygen plasma (Schwarze P3C, Beijing Jiaruntongli Technology Co., Ltd.) at a pressure of 600 mbar for 5 min. Subsequently, a PVA solution (80 mg/mL) was spin-coated at 500 rpm using a spin coater (EZ4, Beijing Tainuo Xinyuan Technology Co., Ltd.) to deposit 500 μL of the solution, followed by annealing at 80 °C for 10 min on a hot plate (V-1515, Dongguan Weitaike Automation Technology Co., Ltd.) to form the blocking dielectric layer (BDL). A gold nanoparticle solution was then spray-coated onto the BDL and air-dried to act as the floating gate (FG) layer. A parylene tunneling dielectric layer (TDL) was deposited using a chemical vapor deposition system (PTP-1V MLD, Baiteng Technology (Suzhou) Co., Ltd.) at 120 °C under a pressure of 3×10^{-2} Pa for 10 h. Thereafter, a 200 μL P3HT solution (8 mg/mL) was spin-coated at 2000 rpm and annealed at 80 °C for 10 min to form the semiconductor layer. Finally, two patterned gold electrodes (30 nm thick, 10 mm in length, with a channel separation of 0.5 mm) were deposited by magnetron sputtering as the source and drain electrodes, thereby completing the device fabrication. During the entire device fabrication process, all annealing steps involving thin films were conducted in a high-purity nitrogen atmosphere. After the spin-coating of the PVA dielectric layer and the P3HT organic semiconductor layer, the devices were transferred into a glovebox filled with high-purity nitrogen and annealed at 80 °C for 10 min. Figure 1(a) illustrates the complete fabrication process flow, and Fig. 1(b) shows the schematic structure of the device. The flexible memory employs a bottom-gate top-contact configuration, sequentially consisting of the semiconductor layer, parylene TDL, FG layer, and PVA BDL.

2.3 Measurement and instruments

In this study, the microstructure of gold nanoparticles was characterized using a JEOL F200 transmission electron microscope (TEM), and elemental analysis was performed via energy-dispersive X-ray spectroscopy (EDS). The electrical and memory characteristics of the FG-OTFT devices were measured using a semiconductor parameter analyzer (4200-SCS, Shenzhen Wanbo Instrument Co., Ltd.). Throughout the testing process, the source electrode was grounded, and all measurements were conducted under ambient conditions. The output characteristics (I_{DS}–V_{DS}) of the FG-OTFT memory were measured under various gate voltages, which were applied from 20 to −60 V in steps of −20 V, while the drain voltage was swept from 0 to −80 V, allowing clear observation of the saturation region. The transfer characteristics (I_{DS}–V_G) were acquired at a constant drain voltage of −60 V, with the gate voltage scanned from 0 to −70 V.

3 Results and discussion

3.1 Film morphologies

The presence of gold nanoparticles (Au NPs) in the floating gate layer was confirmed by transmission electron microscopy (JEOL F200). Figures 1(c) and 1(d) show TEM images of the Au NPs, revealing discrete spherical morphology with a filling density of 36 particles/μm^2. Figure 1(e) displays the EDS elemental mapping image of Au, verifying that its elemental composition corresponds to the particle morphology observed in the TEM images. Statistical analysis of the Au NP size distribution (Fig. 1(f)) indicates an average particle diameter of 10.163 nm with a narrow size distribution, demonstrating good monodispersity. This result provides a crucial foundation for the subsequent formation of a homogeneous floating-gate nanoparticle layer, which is essential for ensuring consistent memory performance.

Au NPs possess excellent chemical inertness, which prevents oxidation and undesirable chemical reactions, thereby ensuring the long-term stability of the floating gate layer during device operation. Additionally, their work function aligns well with the energy levels of the P3HT active layer and dielectric materials (such as Parylene), facilitating the formation of an effective charge injection barrier. This enables efficient and controllable charge trapping and release. Sodium citrate was added to the nanoparticle solution as a stabilizer to ensure good monodispersity of the nanoparticles before spraying. The deposited morphology, confirmed by TEM imaging (Figs. 1(c) and 1(d)), shows that the Au NPs are discretely and spherically distributed without significant agglomeration, successfully forming a discrete floating gate structure. When a programming voltage is applied to the gate, holes from the P3HT channel can tunnel through the thin Parylene layer and be effectively trapped by the Au NPs. Each discrete nanoparticle acts as an independent charge storage node, and due to the nanoscale effect and the potential barrier formed with the surrounding dielectric, the trapped charges exhibit good localization. Furthermore, the thicker PVA blocking layer effectively confines the trapped charges within the floating gate layer, significantly reducing the probability of charge leakage back to the channel through the gate dielectric layer. The low defect density of the Au NPs themselves, along with the clear interface with the dielectric layer, further helps suppress charge relaxation losses and enhances the stability of charge storage.

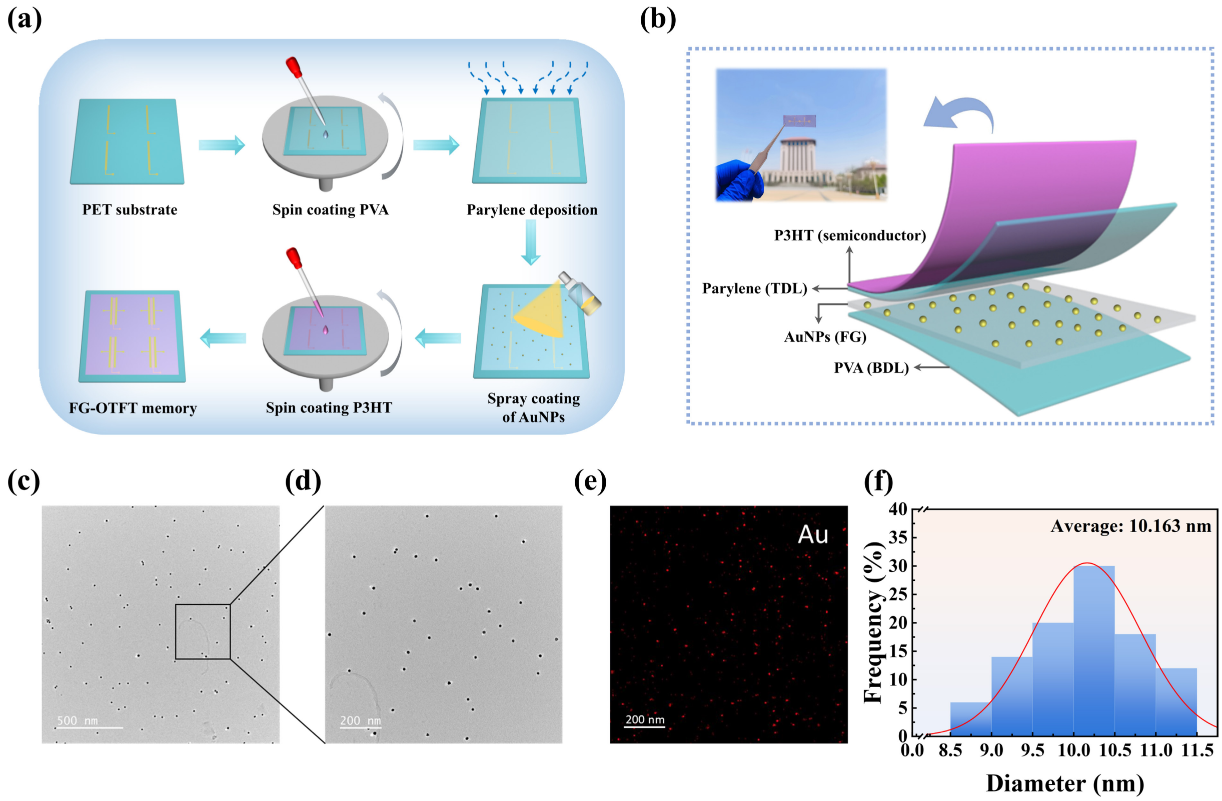

Figure 1 (a) Fabrication process flow of the P3HT-based FG-OTFT memory. (b) Schematic structure of the FG-OTFT memory device. (c) and (d) TEM images of the gold nanoparticles in the floating gate layer of the FG-OTFT memory. (e) EDS elemental mapping image of Au obtained by TEM. (f) Size distribution of gold nanoparticles derived from TEM images.

3.2 Performance testing of the device

A flexible OTFT memory device with a bottom-gate top-contact structure was fabricated, using P3HT as the active layer and Au NPs as the floating gate layer. Figure 2(a) shows a physical image of the as-prepared device. The electrical and memory characteristics of the device were measured by connecting it to a 4200-SCS semiconductor parameter analyzer via a probe station. Since illumination at specific wavelengths can generate carriers in the P3HT layer upon exposure, thereby influencing the programming and erasing processes of the device, uncontrolled variations in external light conditions may introduce undesired effects during electrical measurements. To minimize testing errors, all characterizations were conducted in a dark environment. The electrical performance of the FG-OTFT memory was evaluated by measuring its output and transfer characteristic curves. Figures 2(b) and 2(c) display typical output and transfer characteristics, respectively, which exhibit classical OTFT behaviors. The P-type semiconductor serving as the active layer enables the source-drain current (I_{DS}) to be effectively modulated by the gate-source voltage (V_G). The device demonstrates typical p-channel operation. At low drain-source voltage (V_{DS}), the device operates in the linear region. As V_{DS} increases to approximately 40 V, it enters the saturation region, where I_{DS} increases significantly with higher gate voltage (V_G), indicating effective control of the conduction channel width by the gate bias in the Au NP-based floating-gate memory. During the programming operation, applying a negative gate voltage ($V_G < 0$) enables holes to tunnel from the P3HT channel into the gold nanoparticles and become trapped, leading to an increase in hole concentration within the channel. In subsequent read operations, the trapped charges in the floating gate layer generate an additional local electric field, which aligns with the direction of the applied gate voltage, thereby further enhancing carrier accumulation in the channel. Consequently, under the same read gate voltage, the charges stored in the floating gate effectively modulate the channel conductivity, resulting in a significant increase in the saturation region drain-source current (I_{DS}) as the gate voltage (V_G) increases. This phenomenon not only demonstrates the effective modulation of the channel by the gate voltage but also directly confirms the charge storage effect of the gold nanoparticle floating gate and its active modulation of channel conductance.

The memory characteristics are fundamentally governed by a threshold voltage (V_T) shift, which is controlled by the amount of charge stored in the floating gate layer. The charge storage state can be altered by applying program/erase voltages ($V_{P/E}$). In this study, the memory behavior was investigated by sweeping the gate voltage within a range of ±80 V. The memory window of the device can be quantified as the difference in threshold voltage between the programmed and erased states. Therefore, the transfer characteristic curves in these two states were fitted using the saturation-region drain current expression, as given by Eq. (1) [61]

$$I_{DS} = \frac{\mu C_i W}{2L}(V_G - V_T)^2 \tag{1}$$

where W and L represent the channel width and length of the device, respectively, μ denotes the charge carrier mobility, and C_i refers to the capacitance per unit area of the insulating layer.

Figure 2(d) shows the transfer characteristic curve of the fabricated FG-OTFT memory measured at $V_{DS} = -60$ V. Fitting the transfer curve in the initial state using Eq. (1) yields a threshold

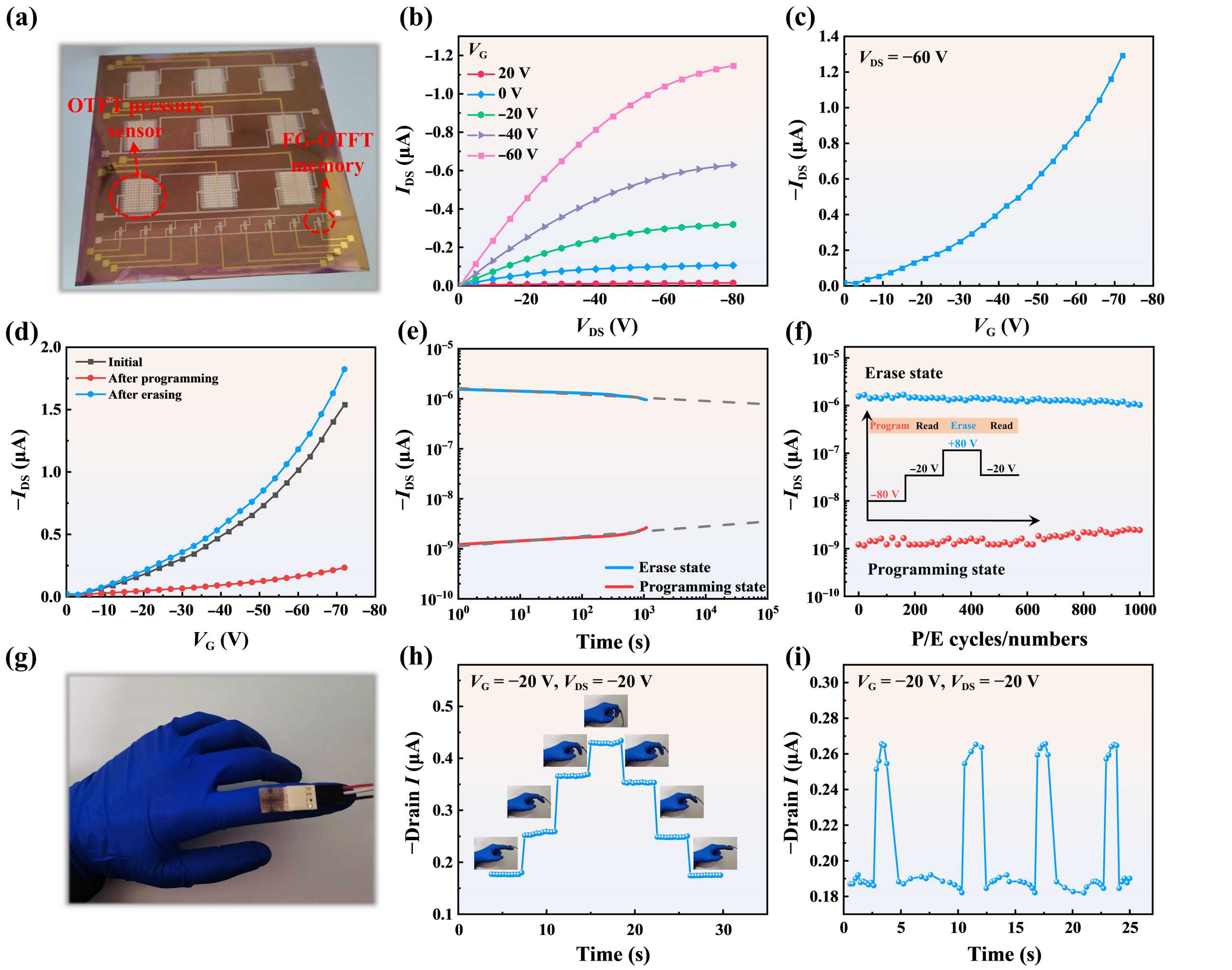

Figure 2 (a) Optical image of the P3HT-based FG-OTFT memory device. (b) Output characteristics of the FG-OTFT memory. (c) Transfer characteristics of the FG-OTFT memory. (d) Transfer characteristics after program/erase operations. (e) Charge retention characteristics of the FG-OTFT memory. (f) Endurance performance under repeated program/erase cycles. (g) A physical image of a flexible pressure sensor integrated onto the finger. (h) Current variations in a pressure sensor attached to a human finger joint during flexion at 0°, 30°, 60°, and 90°. (i) Current variation of the pressure sensor in response to repeated finger pressing.

voltage of 10 V. A programming operation was performed by applying a gate voltage of −80 V for 1 s. The transfer characteristic was measured immediately afterward, corresponding to the "After programming" curve in Fig. 2(d). The fitted threshold voltage after programming increased by 17 V compared to the initial state. Subsequently, an erase operation was conducted by applying V_G = +80 V for 1 s, followed by immediate measurement of the transfer characteristic, shown as the "After erasing" curve in Fig. 2(d). The fitted threshold voltage after erasing decreased by 1 V relative to the initial state. As a result, the FG-OTFT memory exhibited a memory window of 18 V under program/erase voltages of ±80 V. These results demonstrate that the gold nanoparticle-based floating-gate memory can clearly distinguish between two distinct charge storage states. To promote the practical application of this memory in low-power scenarios such as wearable electronics, our future work will focus on significantly reducing its operating voltage. Specifically, organic semiconductor materials with suitable energy levels can be doped into or composited with Parylene to form a graded energy level [62] structure. This facilitates stepwise hole hopping under an external electric field, thereby lowering the overall tunneling barrier and enabling charge injection at lower voltages [63]. Alternatively, the low-voltage storage strategy based on ion migration [64] can be applied to the P3HT sensing-storage system. In practice, the original PVA blocking layer and Parylene tunneling layer can be replaced by an "ion-coupled layer", which may consist of a doped polymer electrolyte. The strong localized electric field generated by ion migration at the interface directly assists charge injection into the floating gate, effectively reducing the injection barrier.

Charge retention time, which characterizes the stability of stored charges in a memory device under programmed and erased states, is a key parameter for evaluating non-volatile memory performance. Figure 2(e) shows the charge retention characteristics of the FG-OTFT memory. Immediately after program/erase operations, the channel current was continuously measured for 10^3 s under a read voltage of V_G = V_{DS} = −20 V, capturing the evolution of the current over time in both states. Fitting of the obtained curves revealed that the memory current on/off ratio decayed to 26% of its initial value after 10^4 s. Based on the fitting results, it is extrapolated that after 10^5 s, the current on/off ratio would decline to approximately 18% of the initial value, indicating a charge retention time of up to 10^5 s. This already meets the requirements for short- to medium-term data buffering in many wearable electronic systems. It is worth noting that the gradual charge loss primarily stems from shallow-level traps in the dielectric layers, while the insufficient interfacial barrier height between the gold nanoparticle floating gate and PVA makes it difficult to fully suppress charge back-tunneling. To enhance long-term retention characteristics, future efforts could focus on optimizing the crystallinity and cross-linking density of PVA to reduce trap state density, or introducing high-dielectric-constant dielectric layers (e.g., TiO_2-doped PVA) to strengthen barrier confinement. Furthermore, adopting gradient dielectric structures or core–shell nanoparticle floating gate designs holds promise for fine-tuning band engineering, thereby significantly extending charge retention time. Endurance testing involves repeated “read–program–erase” cycles to evaluate the device’s operational durability. As shown in Fig. 2(f), the current on/off ratio remained around 4.2×10^2 throughout 1000 cycles, demonstrating robust endurance performance of the device.

The performance of the pressure sensor is crucial for its integration into the sensing-storage system. To evaluate its suitability for detecting physiological skin signals, its pressure response was assessed. As shown in Fig. 2(g), a physical image depicts the pressure sensor attached to the finger. Figure 2(h) presents a bending test, where the current was measured after bending the finger joint to 0°, 30°, 60°, and 90° with the pressure sensor attached. Distinct current variations can be clearly observed. Additionally, current changes were measured after bending the wrist to different angles with the pressure sensor attached, and the results demonstrate significant current variations (Fig. S1 in the Electronic Supplementary Material (ESM)). Furthermore, tests were conducted with the sensor attached to the human throat during intermittent coughing, which also showed clear current changes (Fig. S2 in the ESM). Figure 2(i) demonstrates that applied pressure leads to a significant increase in output current. Additionally, the sensor exhibits clear and reproducible dynamic responses to repeatedly applied finger pressure, confirming its robustness for wearable applications. Figure S3 in the ESM presents the sensitivity calibration curve of the flexible OTFT-based pressure sensor. The maximum sensitivity of the sensor, calculated from the slope of the linear regression fit within the corresponding response region, is determined to be 1.38 kPa^{-1}.

When the FG-OTFT memory and pressure sensor were applied in wearable devices, their fundamental stability was evaluated, including bending endurance tests and environmental temperature tests. The device underwent continuous dynamic bending cycle testing at a bending radius of approximately 8 mm. The test simulated dynamic deformation through manual bending. After completing a certain number of cycles (e.g., 1000, 2000, 3000 cycles), the device was restored to a flat state, and the changes in its memory window and on/off ratio were measured to systematically evaluate the degradation of the device’s electrical performance under mechanical bending. After 3000 bending cycles, the memory window and current on/off ratio of the device decreased slightly, as shown in Fig. 3(a). Additionally, the memory window and on/off ratio were measured over a temperature range of −20 to 60 °C, covering seasonal temperature variations. The results in Fig. 3(b) demonstrate that these parameters remained nearly unaffected by temperature changes. Thus, the transistor memory exhibits excellent mechanical durability after repeated bending and outstanding stability across varying environmental temperatures, confirming its reliable memory performance. Furthermore, the memory windows and the current on/off ratio of 50 devices were measured under program/erase voltages of ±80 V. The 50 devices used for consistency evaluation were fabricated in a single batch on the same flexible PET substrate to assess the within-batch uniformity of the monolithically integrated process developed in this study. The statistical distributions of the memory window and current on/off ratio for these devices are summarized in Figs. 3(c) and 3(d), respectively. The test results indicate that the key performance metrics of the vast majority of devices are satisfactory, demonstrating good within-batch consistency of the solution-based

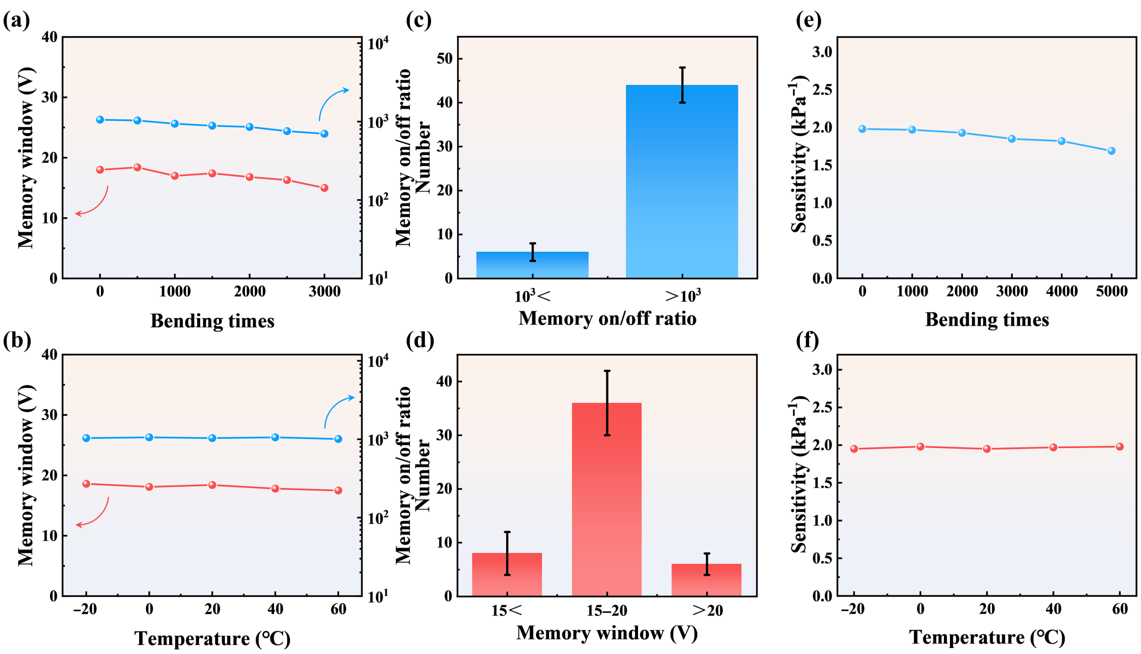

Figure 3 (a) Variation in the memory window and current on/off ratio of the FG-OTFT memory after 3000 bending cycles. (b) Effect of ambient temperature on the memory window and current on/off ratio of the FG-OTFT memory. (c) Statistical distribution of the memory window across 50 FG-OTFT devices. (d) Statistical distribution of the current on/off ratio across 50 FG-OTFT devices. (e) Variation in the sensitivity of the pressure sensor after 5000 bending cycles. (f) Variation of the pressure sensor’s sensitivity with temperature.

Tsinghua University Press | SciOpen

fabrication process. The few outliers observed in the statistical distribution are primarily attributed to film thickness gradient effects at the substrate edges and unavoidable local micro-defects, with their degree of deviation falling within the normal variation range of solution-processed fabrication. This statistical analysis validates, at the device level, the reliable process stability of the proposed integration scheme. To evaluate the sensor's stability, we conducted bending cycle and environmental temperature tests. As shown in Figs. 3(e) and 3(f), the sensor's sensitivity only slightly decreased after 5000 bending cycles and remained stable over a broad temperature range from −20 to 60 °C. These results indicate that the device possesses excellent mechanical and environmental stability, meeting the requirements for wearable applications.

4 Applications

To demonstrate the functionality of the flexible FG-OTFT memory, a pressure sensor array and a 1 × 9 memory array were monolithically integrated on the same flexible PET substrate to validate its perception-storage capability. Based on the aforementioned study, a customized data acquisition circuit was designed to collect signals from both the pressure sensors and the FG-OTFT memory. The acquired data was wirelessly transmitted via Bluetooth low energy (BLE) to a mobile application for remote storage and visualization. Compared with previously reported pressure sensors, the one integrated in our sensing-storage system demonstrates a shorter response time and a wider detection range. The accelerated response capability ensures real-time data transmission, as quantitatively compared in Table S1 in the ESM [65–69]. Simultaneously, the memory module in this integrated system exhibits significantly longer data retention time and superior mechanical flexibility relative to existing memory devices, with the comparative results presented in Table S1 in the ESM [52, 70–73].

The system employs a hierarchical signal processing architecture. At the sensing layer, a 20 V excitation voltage is generated via a digital-to-analog converter (DAC) coupled with a high-voltage operational amplifier to measure the source-drain current of the P3HT OTFT pressure sensor. In the signal conversion layer, programming and erasing operations are performed on the FG-OTFT memory by applying programming/erasing voltages using a 4200-SCS semiconductor parameter analyzer, while the memory state is read through a voltage excitation (also output by a 20 V DAC). At the data processing layer, the source-drain current is converted into a digital signal via an analog-to-digital converter (ADC), and a binary data stream (0/1) is generated after threshold comparison. Finally, the encoded data is transmitted in real-time to a mobile terminal via a BLE module and visualized as ASCII code within a custom-developed Android application. The corresponding ASCII table is provided in Table S2 in the ESM. As illustrated in Fig. 4(a), the wireless perception-storage integrated system primarily consists of an OTFT pressure sensor array, an FG-OTFT memory array, a lower-computer hardware circuit for voltage output and acquisition, and an upper-computer system for data processing and display. When pressure is applied to the OTFT sensor array, the system utilizes the DAC and voltage amplifier to supply a 20 V reading voltage to measure the source-drain current of the transistor-based pressure sensors. Based on the acquired current values, the 4200-SCS analyzer applies program/erase voltages to the FG-OTFT memory for programming/erasing operations. The ADC then converts the source-drain current into

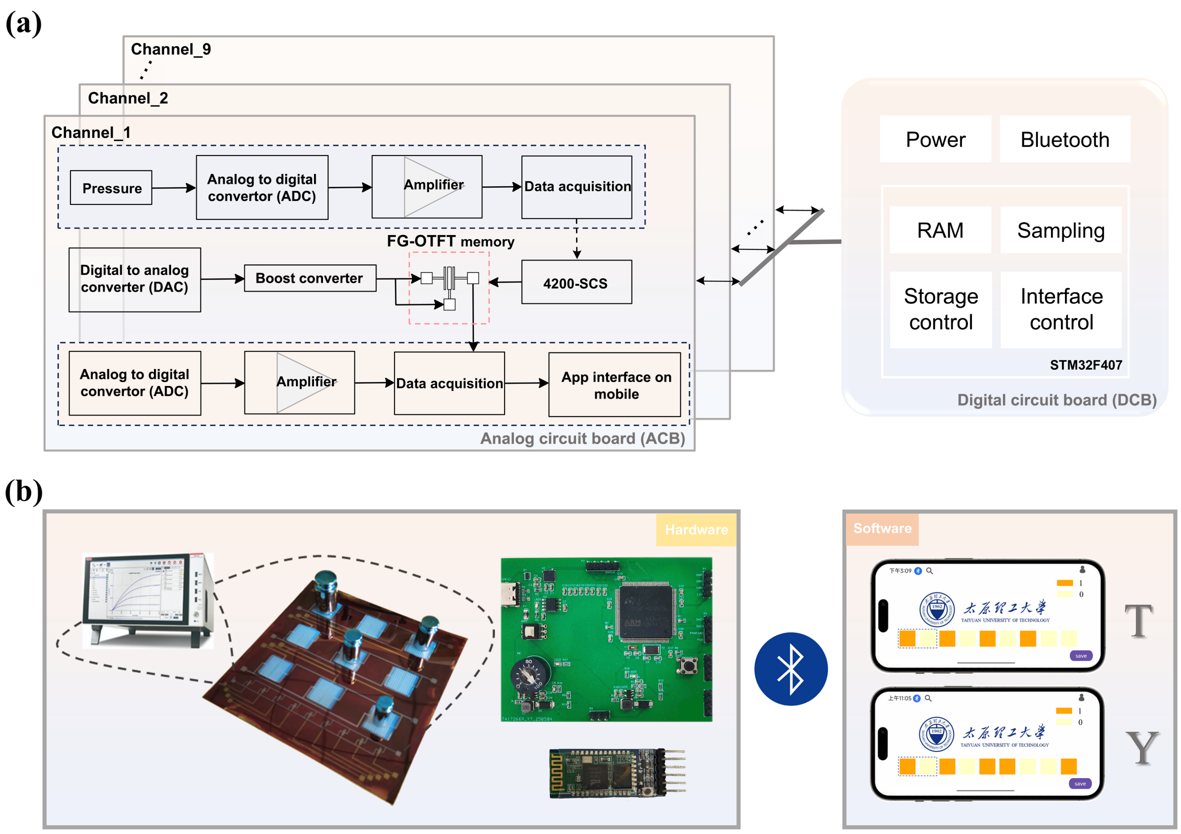

Figure 4 (a) Schematic diagram illustrating the principle of the sensing-storage monolithically integrated system. (b) Detailed physical diagram of the sensing-storage monolithically integrated system and its display on a mobile phone interface.

0/1 data, which are transmitted via Bluetooth to a mobile application for real-time display. Figure 4(a) shows the schematic diagram of the designed monolithic perception-storage system, while Fig. 4(b) displays the physical implementation, including the OTFT pressure sensor array, FG-OTFT memory array, hardware circuitry, Bluetooth module, and mobile application interface.

The term "system" referred to in the text specifically denotes the sensing-storage functional unit, which is a monolithically integrated module comprising a pressure sensor and a floating-gate memory on a unified flexible PET substrate. This integrated unit is entirely fabricated via solution-processable methods, achieving both physical and functional integration of the sensing and storage modules on a flexible platform. Consequently, at the device level, it eliminates the mechanical mismatch and complex interconnections inherent in traditional hybrid rigid-flex integration schemes.

The PCB board shown in Fig. 4(b) serves as the peripheral testing and signal conditioning circuit, designed to provide electrical excitation, signal readout, and wireless transmission functions for the flexible sensing-storage unit. In the practical demonstration, the flexible integrated unit is connected to the PCB via fine wires to verify its system-level operational feasibility. This separated design is adopted for experimental convenience and does not compromise the completeness or independence of the flexible integrated unit itself. In future work, the peripheral circuits could be further flexibilized using flexible electronics technologies to realize a fully flexible integrated system.

To validate the functional characteristics of the monolithic perception-storage integrated system, 20 g weights were first applied at different spatial positions on the sensor array. Experimental results demonstrated that the pressure sensor array generated distinct source–drain current responses corresponding to the applied pressure levels. Based on these current signal characteristics, programming/erasing voltage control was precisely applied to the memory array manually via a 4200-SCS semiconductor parameter analyzer (Fig. 5(a)). As shown in Figs. 5(b)–5(e), the system successfully wrote the 7-bit ASCII codes of four letters "T" (1010100), "Y" (1011001), "U" (1010101), and "T" (1010100)—into the memory array. It is noteworthy that the first two bits in the 9-bit FG-OTFT memory array were specifically designed as check bits ("10"). This design ensures that subsequent memory cells can only perform programming/erasing operations when the verification condition is satisfied. By integrating a Bluetooth transmission module, the system can wirelessly transmit the programming status of the memory cells to a mobile application in real time, enabling visual reading and verification of the data stored in the memory array. This design not only achieves reliable conversion from pressure information to digital encoding but also significantly enhances the observability and operability of system data.

5 Conclusions

In summary, we have developed a P3HT-based, fully solution-processed, sensing-storage monolithically integrated system specifically designed for wearable physiological monitoring applications. The system integrates a flexible OTFT pressure sensor with a floating-gate OTFT memory array on a single PET substrate, thereby eliminating rigid silicon-based memory components and the associated mechanical mismatch and complex interconnects. The memory device displays a large 18 V memory window under ±80 V programming/erasing, long-term charge retention beyond 10^5 s, stable operation after 3000 bending cycles, and excellent device-to-device uniformity, satisfying the requirements for reliable data storage in deformable electronics. The P3HT OTFT pressure sensor provides a broad pressure range (0–40 kPa), a rapid response time of 34 ms, and robust mechanical and environmental stability (up to 5000 bending cycles and −20 to 60 °C). When laminated onto the finger joint, wrist, and human throat, the device produces clear and reproducible current changes in response to finger flexion, wrist bending, and intermittent coughing, confirming its capability for monitoring joint motion and respiratory-related physiological information in real time. By encoding pressure-induced current signals into 7-bit ASCII data within a 1 × 9 memory array, supplemented by two check bits for error control, and wirelessly transmitting these data via Bluetooth to

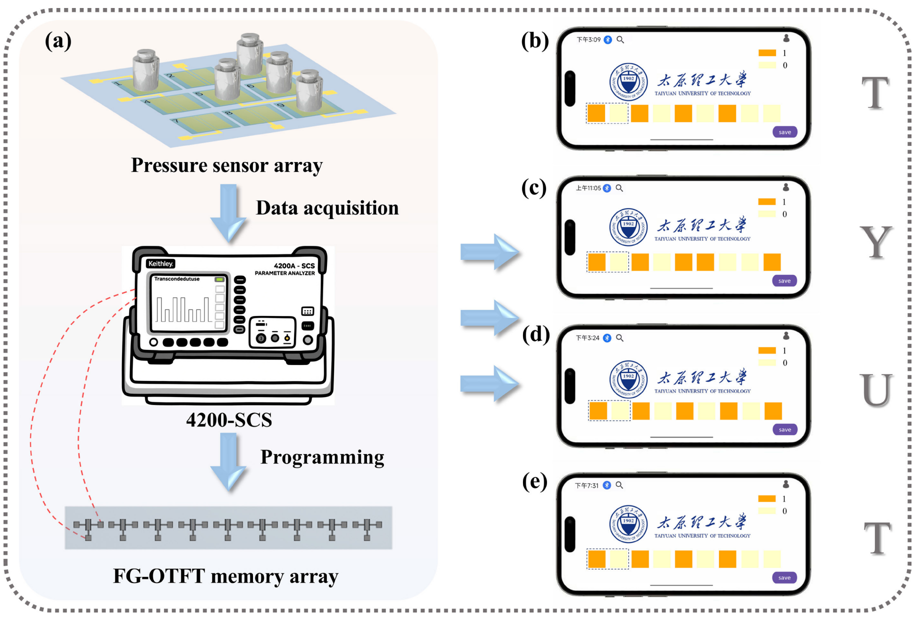

Figure 5 (a) Schematic diagram illustrating the operational process of the monolithic perception–storage system. (b)–(e) Interface displays of the mobile application corresponding to the writing of standard ASCII codes for the characters "T", "Y", "U", and "T" into the memory array, respectively.

a mobile application, the system realizes on-board storage and visual verification of physiological events on a flexible substrate. Benchmarking against previously reported flexible OTFT-based pressure sensors and organic memory devices demonstrates that our integrated platform combines a faster sensing response and extended data retention with mechanical flexibility, offering clear advantages for continuous physiological monitoring. These features position the proposed P3HT-based sensing-storage system as a promising candidate for future electronic-skin technologies and wearable medical electronics. Our future work will focus on optimizing the device fabrication process to enhance performance while reducing the operating voltage from the current ±80 V to a safer and more practical level for wearable applications, along with improving charge retention time to meet the requirements of long-term wearable monitoring.

Electronic Supplementary Material: Supplementary material (Figs. S1–S3 and Tables S1–S2) is available in the online version of this article at https://doi.org/10.26599/NR.2026.94908532.

Data availability

All data needed to support the conclusions in the paper are presented in the manuscript and the Electronic Supplementary Material. Additional data related to this paper may be requested from the corresponding author upon request.

Acknowledgements

This work was supported by Fundamental Research Program of Shanxi Province (Nos. 202403021221067 and 202403021221203), Patent Transformation Program of Shanxi Province (Nos. 202405020 and 202401004), and China Scholarship Council funding (No. 202206935020).

Declaration of competing interest

All the contributing authors report no conflict of interests in this work.

Author contribution statement

Y. W. L.: Data curation, visualization, writing – original draft. Q. L.: Conceptualization, methodology, funding acquisition, writing – review & editing. L. F. D.: Funding acquisition, writing – review & editing. Y. Z. C.: Validation. H. G.: Supervision. J. N. M.: Supervision. T. M.: Conceptualization, validation. S. B. S.: Validation.

Use of AI statement

None.

References

[1] Chen, L. R.; Xu, Y. Q.; Liu, Y. F.; Wang, J.; Chen, J. W.; Chang, X. H.; Zhu, Y. T. Flexible and transparent electronic skin sensor with sensing capabilities for pressure, temperature, and humidity. *ACS Appl. Mater. Interfaces* **2023**, *15*, 24923–24932.

[2] Kim, S. W.; Lee, J. H.; Ko, H. J.; Lee, S.; Bae, G. Y.; Kim, D.; Lee, G.; Lee, S. G.; Cho, K. Mechanically robust and linearly sensitive soft piezoresistive pressure sensor for a wearable human-robot interaction system. *ACS Nano* **2024**, *18*, 3151–3160.

[3] Hou, K. X.; Zhao, S. P.; Wang, D. P.; Zhao, P. C.; Li, C. H.; Zuo, J. L. A puncture-resistant and self-healing conductive gel for multifunctional electronic skin. *Adv. Funct. Mater.* **2021**, *31*, 2107006.

[4] Núñez, C. G.; Manjakkal, L.; Dahiya, R. Energy autonomous electronic skin. *npj Flex. Electron.* **2019**, *3*, 1.

[5] Choi, S. B.; Noh, T.; Jung, S. B.; Kim, J. W. Stretchable piezoresistive pressure sensor array with sophisticated sensitivity, strain-insensitivity, and reproducibility. *Adv. Sci.* **2024**, *11*, 2405374.

[6] Pei, H. R.; Jing, J. J.; Chen, Y. H.; Guo, J. J.; Chen, N. 3D printing of PVDF-based piezoelectric nanogenerator from programmable metamaterial design: Promising strategy for flexible electronic skin. *Nano Energy* **2023**, *109*, 108303.

[7] Yuan, J. X.; Li, Q.; Ding, L. F.; Shi, C. C.; Wang, Q.; Niu, Y. L.; Xu, C. Y. Carbon black/multi-walled carbon nanotube-based, highly sensitive, flexible pressure sensor. *ACS Omega* **2022**, *7*, 44428–44437.

[8] Chowdhury, A. H.; Jafarizadeh, B.; Baboukani, A. R.; Pala, N.; Wang, C. L. Monitoring and analysis of cardiovascular pulse waveforms using flexible capacitive and piezoresistive pressure sensors and machine learning perspective. *Biosens. Bioelectron.* **2023**, *237*, 115449.

[9] Dahiya, A. S.; Zumeit, A.; Christou, A.; Loch, A. S.; Purushothaman, B.; Skabara, P. J.; Dahiya, R. Printing semiconductor-based devices and circuits for flexible electronic skin. *Appl. Phys. Rev.* **2024**, *11*, 041334.

[10] Kameda, M.; Seki, H.; Makoshi, T.; Amao, Y.; Nakakita, K. A fast-response pressure sensor based on a dye-adsorbed silica nanoparticle film. *Sens. Actuators B: Chem.* **2012**, *171–172*, 343–349.

[11] Zhang, Y.; Hu, Y. G.; Zhu, P. L.; Han, F.; Zhu, Y.; Sun, R.; Wong, C. P. Flexible and highly sensitive pressure sensor based on microdome-patterned PDMS forming with assistance of colloid self-assembly and replica technique for wearable electronics. *ACS Appl. Mater. Interfaces* **2017**, *9*, 35968–35976.

[12] Baek, J.; Shan, Y.; Mylvaganan, M.; Zhang, Y. X.; Yang, X. X.; Qin, F.; Zhao, K. J.; Song, H. W.; Mao, H. C.; Lee, S. Mold-free manufacturing of highly sensitive and fast-response pressure sensors through high-resolution 3d printing and conformal oxidative chemical vapor deposition polymers. *Adv. Mater.* **2023**, *35*, 2304070.

[13] Yang, C. F.; Li, L. L.; Zhao, J. X.; Wang, J. J.; Xie, J. X.; Cao, Y. P.; Xue, M. Q.; Lu, C. H. Highly sensitive wearable pressure sensors based on three-scale nested wrinkling microstructures of polypyrrole films. *ACS Appl. Mater. Interfaces* **2018**, *10*, 25811–25818.

[14] Li, Y.; Wu, G. F.; Song, G.; Lu, S. H.; Wang, Z. Z.; Sun, H.; Zhang, Y.; Wang, X. J. Soft, pressure-tolerant, flexible electronic sensors for sensing under harsh environments. *ACS Sens.* **2022**, *7*, 2400–2409.

[15] Li, Y.; Zhang, Z. Z.; Du, S. L.; Zong, S. C.; Ning, Z. J.; Yang, F. L. Highly sensitive biomimetic crack pressure sensor with selective frequency response. *ACS Sens.* **2024**, *9*, 3057–3065.

[16] Jeong, Y.; Park, J.; Lee, J.; Kim, K.; Park, I. Ultrathin, biocompatible, and flexible pressure sensor with a wide pressure range and its biomedical application. *ACS Sens.* **2020**, *5*, 481–489.

[17] Wang, W. V.; Zhang, Y. M.; Li, X. Y.; Chen, Z. Z.; Wu, Z. H.; Zhang, L.; Lin, Z. W.; Zhang, H. L. High performance nonvolatile organic field-effect transistor memory devices based on pyrene diimide derivative. *InfoMat* **2021**, *3*, 814–822.

[18] Zhang, G. C.; Ma, C.; Wu, X. M.; Zhang, X. H.; Gao, C. S.; Chen, H. P.; Guo, T. L. Transparent organic nonvolatile memory and volatile synaptic transistors based on floating gate structure. *IEEE Electron Device Lett.* **2022**, *43*, 733–736.

[19] Cui, X. H.; Jiang, Y.; Hu, L.; Cao, M.; Xie, H. Y.; Zhang, X. C.; Huang, F. L.; Xu, Z. G.; Zhu, Y. T. Synergistically microstructured flexible pressure sensors with high sensitivity and ultrawide linear range for full-range human physiological monitoring. *Adv. Mater. Technol.* **2023**, *8*, 2200609.

[20] Kang, F.; Zhang, W. Q.; Liu, M. L.; Liu, F.; Jia, Z. X.; Jia, D. M.

Highly flexible and sensitive Ti_3C_2 MXene@polyurethane composites for piezoresistive pressure sensor. *J. Mater. Sci.* **2022**, *57*, 12894–12902.
[21] Wang, M.; Zhang, H.; Wu, H.; Ma, S. Q.; Ren, L.; Liang, Y. H.; Liu, C. B.; Han, Z. W. Bioinspired flexible piezoresistive sensor for high-sensitivity detection of broad pressure range. *Bio-Des. Manuf.* **2023**, *6*, 243–254.
[22] Hong, S. H.; Chen, T. H.; Wang, G. R.; Popovic, S. M.; Filleter, T.; Naguib, H. E. Room-temperature self-healing polysiloxane networks for highly sensitive piezoresistive pressure sensor with microdome structures. *Chem. Eng. J.* **2023**, *471*, 144429.
[23] Geng, J. C.; Li, Q.; Liu, Z. T.; Ding, L. F.; Su, F. L.; Ullan, R.; Minami, T.; Sang, S. B. Multifunctional electronic glove via 3D printing for dual-mode pressure-temperature sensing and interactive applications. *Chem. Eng. J.* **2025**, *522*, 167129.
[24] Chang, Z. Q.; Li, Q.; Ding, L. F.; Chen, Y. M.; Li, X. W.; Li, L. L.; Ullan, R.; Jian, A. Q.; Zhang, Q.; Sang, S. B. Tailoring fractal structure via 3D printing to achieve flexible stretchable electrodes based on Ecoflex/CNT/CF. *Mater. Today Commun.* **2024**, *38*, 107721.
[25] Tang, W. T.; Lv, B. H.; Pei, Z.; Fu, Z. Y.; Zhang, C. Y.; Zeng, Y. H.; Wang, K.; Zhang, Q. Bioinspired soft pressure sensors with interlocked structures based on 3D Printing methods. *ACS Appl. Polym. Mater.* **2024**, *6*, 11575–11585.
[26] Wang, K.; Ma, J. N.; Zhao, Q.; Zhang, J. H.; Zhang, K. D.; Zhang, Y.; Wang, L.; Sang, S. B. $Ti_3C_2T_x$ MXene-based multifunctional wearable integrated sensor for simultaneous detection of humidity and pressure stimuli. *Sens. Actuators B: Chem.* **2025**, *442*, 138147.
[27] Luo, J. N.; Wu, J. Z.; Zheng, X. P.; Xiong, H. R.; Lin, L.; Liu, C.; Liu, H. D.; Tang, H.; Liu, H. F.; Han, F. et al. Microcavity assisted graphene pressure sensor for single-vessel local blood pressure monitoring. *Nano Res.* **2024**, *17*, 10058–10068.
[28] Ji, J. J.; Huang, Z. L.; Xie, H. W.; Wang, Y. Z.; Chen, T.; Yang, L. P.; Jiang, Y.; Liu, J.; Cheng, D.; Wu, T. L. et al. Stretchable multimodal sensor arrays for hardness perception in bionic skin. *Nano Res.* **2025**, *18*, 94907759.
[29] Amna, B.; Ozturk, T. Organic field-effect transistor-based sensors: Recent progress, challenges and future outlook. *J. Mater. Chem. C* **2025**, *13*, 8354–8424.
[30] Wang, X. Y.; Yin, Z. G.; Liu, C. D.; Liu, Y. T.; Ma, Y. L.; Zheng, Q. D. Low-voltage flexible organic transistors utilizing passivated polyelectrolyte dielectrics for tactile sensing and braille recognition. *J. Colloid Interface Sci.* **2025**, *691*, 137417.
[31] Yeo, S. Y.; Park, S.; Yi, Y. J.; Kim, D. H.; Lim, J. A. Highly sensitive flexible pressure sensors based on printed organic transistors with centro-apically self-organized organic semiconductor microstructures. *ACS Appl. Mater. Interfaces* **2017**, *9*, 42996–43003.
[32] Jeong, D.; Jang, S. Y.; Roh, S.; Choi, J. H.; Seo, I. J.; Lee, J. H.; Kim, J.; Kwon, I.; Jung, Y.; Hwang, J. et al. Sprayable hydrogel with optical mRNA nanosensors for Real-Time monitoring and healing of diabetic wounds. *Chem. Eng. J.* **2024**, *493*, 152711.
[33] Yi, Q.; Najafikhoshnoo, S.; Das, P.; Noh, S.; Hoang, E.; Kim, T.; Esfandyarpour, R. All-3D-printed, flexible, and hybrid wearable bioelectronic tactile sensors using biocompatible nanocomposites for health monitoring. *Adv. Funct. Technol.* **2022**, *7*, 2101034.
[34] Abramson, A.; Chan, C. T.; Khan, Y.; Mermin-Bunnell, A.; Matsuhisa, N.; Fong, R.; Shad, R.; Hiesinger, W.; Mallick, P.; Gambhir, S. S. et al. A flexible electronic strain sensor for the real-time monitoring of tumor regression. *Sci. Adv.* **2022**, *8*, eabn6550.
[35] Yu, Y. D.; Zhu, W.; Zhou, J.; Guo, Z. P.; Liu, Y. T.; Deng, Y. Wearable respiration sensor for continuous healthcare monitoring using a micro-thermoelectric generator with rapid response time and chip-level design. *Adv. Mater. Technol.* **2022**, *7*, 2101416.
[36] Wang, L. L.; Jiang, K.; Shen, G. Z. Wearable, implantable, and interventional medical devices based on smart electronic skins. *Adv. Mater. Technol.* **2021**, *6*, 2100107.
[37] Wang, L. L.; Wang, D. P.; Wang, K.; Jiang, K.; Shen, G. Z. Biocompatible MXene/chitosan-based flexible bimodal devices for real-time pulse and respiratory rate monitoring. *ACS Mater. Lett.* **2021**, *3*, 921–929.
[38] Zhao, X.; Zhang, Z.; Xu, L. X.; Gao, F. F.; Zhao, B.; Ouyang, T.; Kang, Z.; Liao, Q. L.; Zhang, Y. Fingerprint-inspired electronic skin based on triboelectric nanogenerator for fine texture recognition. *Nano Energy* **2021**, *85*, 106001.
[39] Zhao, J. Q.; Lin, Y. J.; Wu, J. B.; Nyein, H. Y. Y.; Bariya, M.; Tai, L. C.; Chao, M. H.; Ji, W. B.; Zhang, G.; Fan, Z. Y. et al. A fully integrated and self-powered smartwatch for continuous sweat glucose monitoring. *ACS Sens.* **2019**, *4*, 1925–1933.
[40] Zhang, J. H.; Chen, J. X.; Li, M.; Ge, Y. X.; Wang, T. T.; Shan, P.; Mao, X. L. Design, fabrication, and implementation of an array-type MEMS piezoresistive intelligent pressure sensor system. *Micromachines* **2018**, *9*, 104.
[41] Wang, W.; Han, J. H.; Ying, J.; Xiang, L. Y.; Xie, W. F. Effect of tunneling layers on the performances of floating-gate based organic thin-film transistor nonvolatile memories. *Appl. Phys. Lett.* **2014**, *105*, 123303.
[42] Wu, C.; Wang, W.; Song, J. F. Molecular floating-gate organic nonvolatile memory with a fully solution processed core architecture. *Appl. Phys. Lett.* **2016**, *109*, 223301.
[43] Xu, T.; Guo, S. X.; Qi, W. H.; Li, S. Z.; Xu, M. L.; Xie, W. F.; Wang, W. High-performance flexible organic thin-film transistor nonvolatile memory based on molecular floating-gate and *pn*-heterojunction channel layer. *Appl. Phys. Lett.* **2020**, *116*, 023301.
[44] Li, Q.; Li, X. W.; Ding, L. F.; Li, Y. W.; Ma, J. N.; Sang, S. B.; Minami, T. Organic photodetectors achieving UV-visible broadband detection via P3HT-OFET epitaxial integration. *ACS Appl. Electron. Mater.* **2025**, *7*, 6166–6176.
[45] Fujisaki, Y.; Koga, H.; Nakajima, Y.; Nakata, M.; Tsuji, H.; Yamamoto, T.; Kurita, T.; Nogi, M.; Shimidzu, N. Transparent nanopaper-based flexible organic thin-film transistor array. *Adv. Funct. Mater.* **2014**, *24*, 1657–1663.
[46] Sang, S. B.; Li, L. L.; Li, Q.; Ding, L. F.; Li, X. W.; Chang, Z. Q.; Chen, Y. M.; Ullan, R.; Ma, J. N.; Ji, J. L. A high-performance organic thin-film transistor with Parylene/PMMA bilayer insulation based on P3HT. *iScience* **2024**, *27*, 109724.
[47] Choi, J.; Lee, C.; Kang, J.; Lee, C.; Lee, S. M.; Oh, J.; Choi, S. Y.; Im, S. G. A sub-20 nm organic/inorganic hybrid dielectric for ultralow-power organic thin-film transistor (OTFT) with enhanced operational stability. *Small* **2022**, *18*, 2203165.
[48] Wu, X. C.; Chen, S. Y.; Jiang, L. L.; Wang, X. H.; Qiu, L. Z.; Zheng, L. Highly sensitive, low-energy-consumption biomimetic olfactory synaptic transistors based on the aggregation of the semiconductor films. *ACS Sens.* **2024**, *9*, 2673–2683.
[49] Janićijević, Ž.; Baraban, L. Integration strategies and formats in field-effect transistor chemo- and biosensors: A critical review. *ACS Sens.* **2025**, *10*, 2431–2452.
[50] Abe, H.; Hattori, R.; Nagase, T.; Higashinakaya, M.; Tazuhara, S.; Shiono, F.; Kobayashi, T.; Naito, H. Enhanced performance of solution-processable floating-gate organic phototransistor memory for organic image sensor applications. *Appl. Phys. Express* **2021**, *14*, 041007.
[51] Higashinakaya, M.; Nagase, T.; Abe, H.; Hattori, R.; Tazuhara, S.; Kobayashi, T.; Naito, H. Electrically programmable multilevel nonvolatile memories based on solution-processed organic floating-gate transistors. *Appl. Phys. Lett.* **2021**, *118*, 103301.
[52] Nam, T. U.; Vo, N. T. P.; Jeong, M. W.; Jung, K. H.; Lee, S. H.; Lee, T. I.; Oh, J. Y. Intrinsically stretchable floating gate memory transistors for data storage of electronic skin devices. *ACS Nano* **2024**, *18*, 14558–14568.
[53] Yang, W. C.; Lin, Y. C.; Liao, M. Y.; Hsu, L. C.; Lam, J. Y.; Chuang, T. H.; Li, G. S.; Yang, Y. F.; Chueh, C. C.; Chen, W. C.

Comprehensive non-volatile photo-programming transistor memory via a dual-functional perovskite-based floating Gate. *ACS Appl. Mater. Interfaces* **2021**, *13*, 20417–20426.
[54] Chen, Z. C.; Chen, S.; Jiang, T. H.; Chen, S.; Jia, R. F.; Xiao, Y. L.; Pan, J.; Jie, J. S.; Zhang, X. J. A floating-gate field-effect transistor memory device based on organic crystals with a built-in tunneling dielectric by a one-step growth strategy. *Nanoscale* **2024**, *16*, 3721–3728.
[55] Kim, C.; Song, J. M.; Lee, J. S.; Lee, M. J. All-solution-processed nonvolatile flexible nano-floating gate memory devices. *Nanotechnology* **2014**, *25*, 014016.
[56] Jang, S.; Jee, E.; Choi, D.; Kim, W.; Kim, J. S.; Amoli, V.; Sung, T.; Choi, D.; Kim, D. H.; Kwon, J. Y. Ultrasensitive, low-power oxide transistor-based mechanotransducer with microstructured, deformable ionic dielectrics. *ACS Appl. Mater. Interfaces* **2018**, *10*, 31472–31479.
[57] Wang, Z. W.; Guo, S. J.; Li, H. W.; Wang, B.; Sun, Y. T.; Xu, Z. Y.; Chen, X. S.; Wu, K. J.; Zhang, X. T.; Xing, F. F. et al. The semiconductor/conductor interface piezoresistive effect in an organic transistor for highly sensitive pressure sensors. *Adv. Mater.* **2019**, *31*, 1805630.
[58] Sun, Q. J.; Li, T.; Wu, W.; Venkatesh, S.; Zhao, X. H.; Xu, Z. X.; Roy, V. A. L. Printed high-*k* dielectric for flexible low-power extended gate field-effect transistor in sensing pressure. *ACS Appl. Electron. Mater.* **2019**, *1*, 711–717.
[59] Cheng, G. Y.; Xu, H. T.; Gao, N. F.; Zhang, M. Q.; Gao, H. L.; Sun, B. H.; Gu, M. X.; Yu, L. Y.; Lin, Y. C.; Liu, X. Q. et al. Carbon nanotubes field-effect transistor pressure sensor based on three-dimensional conformal force-sensitive gate modulation. *Carbon* **2023**, *204*, 456–464.
[60] Li, Q.; Li, Y. W.; Ding, L. F.; Li, X. W.; Ma, J. N.; Minami, T.; Sang, S. B. Structural optimization of field-effect modulated P3HT OTFT flexible pressure sensors for high sensitivity and rapid response. *Microchem. J.* **2025**, *215*, 114484.
[61] Hao, R. F.; Yue, Y. F.; Li, L. L.; Ji, J. L.; Zhang, Q.; Ding, L. F.; Sang, S. B.; Li, Q. P3HT-based organic field effect transistor for low-cost, label-free detection of immunoglobulin G. *J. Biotechnol.* **2022**, *359*, 75–81.
[62] Lyu, Y. K.; Ji, Z. T.; He, T.; Lu, Z. D.; Zhang, W. H. Automated pick-and-place of single nanoparticle using electrically controlled low-surface energy nanotweezer. *AIP Adv.* **2021**, *11*, 035219.
[63] Wu, F. C.; Li, B. J.; Chou, W. Y.; Cheng, H. L. Multifunctional interfacial layers from a one-step process for effective charge capturing and erasing in low-voltage-driven organic thin-film transistors. *ACS Appl. Electron. Mater.* **2020**, *2*, 1413–1420.
[64] Liu, C. D.; Yin, Z. G.; Liu, Y. T.; Zheng, Q. D. Flexible polyelectrolyte hybrid dielectrics for multilevel nonvolatile low-voltage organic transistor memories. *Chem. Eng. J.* **2025**, *504*, 158625.
[65] Zhao, J. Q.; Guo, H.; Pang, Y. K.; Xi, F. B.; Yang, Z. W.; Liu, G. X.; Guo, T.; Dong, G. F.; Zhang, C.; Wang, Z. L. Flexible organic tribotronic transistor for pressure and magnetic sensing. *ACS Nano* **2017**, *11*, 11566–11573.
[66] Kyaw, A. K. K.; Loh, H. H. C.; Yan, F.; Xu, J. W. A polymer transistor array with a pressure-sensitive elastomer for electronic skin. *J. Mater. Chem. C* **2017**, *5*, 12039–12043.
[67] Baek, S.; Lee, Y.; Baek, J.; Kwon, J.; Kim, S.; Lee, S.; Strunk, K. P.; Stehlin, S.; Melzer, C.; Park, S. M. et al. Spatiotemporal measurement of arterial pulse waves enabled by wearable active-matrix pressure sensor arrays. *ACS Nano* **2022**, *16*, 368–377.
[68] Yin, M. J.; Yin, Z. G.; Zhang, Y. X.; Zheng, Q. D.; Zhang, A. P. Micropatterned elastic ionic polyacrylamide hydrogel for low-voltage capacitive and organic thin-film transistor pressure sensors. *Nano Energy* **2019**, *58*, 96–104.
[69] Liu, Z. Y.; Yin, Z. G.; Wang, J. B.; Zheng, Q. D. Polyelectrolyte dielectrics for flexible low-voltage organic thin-film transistors in highly sensitive pressure sensing. *Adv. Funct. Mater.* **2019**, *29*, 1806092.
[70] Jung, J. H.; Kim, S.; Kim, H.; Park, J.; Oh, J. H. High-performance flexible organic nano-floating gate memory devices functionalized with cobalt ferrite nanoparticles. *Small* **2015**, *11*, 4976–4984.
[71] Li, Q. Y.; Li, T. T.; Zhang, Y. T.; Chen, Z. L.; Li, Y. F.; Jin, L. F.; Zhao, H. L.; Li, J.; Yao, J. Q. Photoerasable organic field-effect transistor memory based on a one-step solution-processed hybrid floating gate layer. *J. Phys. Chem. C* **2020**, *124*, 23343–23351.
[72] Jung, S. W.; Koo, J. B.; Park, C. W.; Na, B. S.; Park, N. M.; Oh, J. Y.; Moon, Y. G.; Lee, S. S.; Koo, K. W. Non-volatile organic ferroelectric memory transistors fabricated using rigid polyimide islands on an elastomer substrate. *J. Mater. Chem. C* **2016**, *4*, 4485–4490.
[73] Moon, B. J.; Song, Y. S.; Son, D.; Yang, H. Y.; Bae, S.; Lee, S. K.; Lee, S. H.; Kim, T. W. Implementation of photosynaptic and electrical memory functions in organic nano-floating-gate transistors via a perovskite-nanocrystal-based nanocomposite tunneling layer. *Small Sci.* **2023**, *3*, 2300068.